Composite Structures 93 (2011) 2861–2873

Contents lists available at ScienceDirect

Composite Structures

journal homepage: www.elsevier.com/locate/compstruct

Surface stress and strain fields on compressed panels of corrugated board boxes. An experimental analysis by using Digital Image Stereocorrelation

J. Viguié [a], P.J.J. Dumont [a,*], L. Orgéas [b], P. Vacher [c], I. Desloges [a], E. Mauret [a]

[a] Laboratoire de Génie des Procédés Papetiers (LGP2), CNRS/Institut polytechnique de Grenoble (Grenoble INP), 461 rue de la Papeterie, BP 65, 38402 Saint-Martin-d'Hères cedex, France
[b] Laboratoire Sols-Solides-Structures-Risques (3SR), CNRS/Université de Grenoble (Grenoble INP – UJF), BP 53, 38041 Grenoble cedex 9, France
[c] Laboratoire SYMME, Université de Savoie, Polytech Savoie, Domaine Universitaire, BP 80439, 74994 Annecy-le-Vieux, France

ARTICLE INFO

Article history:
Available online 25 May 2011

Keywords:
Corrugated board
Digital Image Correlation
Compression
Buckling behaviour
Orthotropic properties
Residual stress

ABSTRACT

The complex behaviour of corrugated board packages under compression loading is investigated in this work. Original experimental data are obtained by using a Digital Image Stereocorrelation technique for measuring the displacement and strain fields of the panels' outer liner of the tested boxes. The stress field is also estimated by accounting for the anisotropic mechanical behaviour of the outer liner, its residual stress state induced by the processing of the corrugated board and the effects of box manufacturing operations and compression. Results show that these fields are extremely heterogeneous on the panels' surface. Most stressed areas are located along the panels' edges. The elastic limit of the outer liner is reached quite soon during compression. Box geometry and panel flaps are of primary importance on the observed phenomena. This approach delivers useful information to improve kinematic and constitutive assumptions for buckling and post-buckling models of boxes or thin-walled sandwich structures.

1. Introduction

There is an increasing demand in G-flute corrugated boards (also called nano-flute corrugated boards), which tend to replace other lightweight packaging materials such as folding boards or plastics. Boxes have to withstand significant compression loading conditions during carriage and storage. In order to evaluate their structural performance, the box compression test is the most currently performed experiment. It consists in compressing an empty container between two parallel plates at a constant velocity. Usually, it is observed that buckling phenomena are localized in the box panels, which bulge out during compression. At the maximum recorded compression force, the deformation localises around the box corners where creases appear and develop. This maximum force is defined as the quasi-static compression strength of the box. The prediction of such strength is the main topic of interest of past and current research works. Some authors strengthened their efforts to obtain a description of the buckling and post-buckling behaviour of individual board panels [1–3]. Nordstrand [3] used an elastic and orthotropic description of the mechanical behaviour up to the failure. The chosen failure criterion was the Tsai–Wu criterion for a plane stress case, which accounts for anisotropic strengths and different strengths in tension and compression loading situations. Besides, the compression behaviour of boxes was studied by McKee et al. [4] and Urbanik [5], who defined semi-empirical formula to predict the box compression strength, as well as by Beldie et al. [6] and Biancolini and Brutti [7] by the finite element method (FEM). But, comparisons of these models with experimental results remain somewhat scarce and limited.

Some full-field optical techniques for displacement or strain measurements were occasionally used in order to characterise the mechanical behaviour of papers or paperboards [2,8,9] subjected to various loading conditions. In particular, Allansson and Svard [2] used a Digital Speckle Photography technique to measure the out-of-plane displacement of a panel loaded in compression using a specially designed supporting frame. Despite its interest, this technique gave only access to rather limited information on the displacement field, *i.e.* a component of the displacement field. Thorpe and Choi [8] made an attempt to measure the strains on surfaces of box panels loaded in compression in the case of convex and concave buckling by using a classical Digital Image Correlation technique. They showed that the in-plane shear strains are significant in the corner regions. However, measurements were only performed in 2D, so that the information they gained on the strain field was incomplete: *e.g.* the contribution of the gradients of the out-of-plane displacement to the strain components could not be assessed. This could be particularly inadequate when dealing with buckling problems.

During the last decade, the DIC techniques have been increasingly developed. It is now possible to measure the 3D displacement

* Corresponding author. Tel.: +33 476826921.
E-mail address: pierre.dumont@grenoble-inp.fr (P.J.J. Dumont).

0263-8223/$ - see front matter © 2011 Elsevier Ltd. All rights reserved.
doi:10.1016/j.compstruct.2011.05.018

field and the surface strain field of any 3D object by the digital image stereocorrelation technique (DISC) [10,11]. In this paper, the first objective is to describe the full 3D displacement field and the related strain field of a box panel, during compression using this 3D DIC technique. The second objective is to determine the full stress field in the outer liner, by considering the residual stresses which result from the corrugated board manufacturing, the elastic stresses which result from the box manufacturing and the elastic stresses which result from the box compression. The last objective is to emphasise the influence of the box geometry on the compression behaviour.

In the first section of this paper, technical aspects related to the box manufacturing, the measurement of the residual stresses, the evaluation of the parameters of the linear orthotropic elastic model of the outer liner, the compression test and the 3D imaging technique are given. In the second section, the initial displacement field and the associated strain field in the surface of a box panel, which result from the box manufacturing, are described. Thereafter, the displacement and strain fields during the box compression are presented. Finally, the stress field in the outer liner is assessed and its evolution is described. In the last section, the influence of the flaps and box dimensions on the buckling and post-buckling behaviour are discussed and some humble optimization routes are proposed.

2. Materials, specimens and experimental procedure

2.1. G-flute corrugated board and box manufacturing

The material used in this study is a double-faced corrugated board with a G profile whose typical dimensions are shown in Fig. 1a. This material has a nominal thickness e of 0.78 mm and an average basis weight of 450 g/m^2. It is composed of a outer liner, a corrugated core and an inner liner which are respectively a 160 g/m^2 kraftliner, a 110 g/m^2 corrugating medium and a 140 g/m^2 testliner. These papers are glued together using a starch-based adhesive. Tested boxes had a square base. The box blanks were drawn using the software ArtiosCad 5.2. They were cut and creased in a Kongsberg XL22 cutting table. As shown in Fig. 1b and c, the box blank includes panels, flaps, scores and a manufacturer joint. The crease depth was chosen equal to 1 mm. The box dimensions are referred to as a for its height and b for its length and depth. Once the box was erected and glued, the inner and outer flaps covered completely the top and bottom box surfaces. Note that the flutes are vertical in the box panels: this means that the cross-direction of the corrugated board is aligned along the compression axis. Note that the machine direction of the panels is referred to as the $\underline{\mathbf{e}}_x$ direction in the following and the cross direction of panels is referred to as the $\underline{\mathbf{e}}_y$ direction.

2.2. In-plane elastic constants of the outer liner

In order to estimate the stress field in the outer liner, the in-plane elastic constants of the outer liner were measured. Besides, a Tsai–Wu yield surface was built by identifying the yield points on the stress–strain curves. As it is not the main subject of this paper, the procedures which were used in Viguié [12] are only briefly exposed here. Two kinds of mechanical tests were carried out on rectangular samples: simple tensile test and plane strain compression test. Simple tensile tests were performed following the Tappi T 404 standard. For performing plane strain compression tests, a special setup prevented the sample buckling. Tested samples had various orientations $\theta = (\underline{\mathbf{e}}_1, \underline{\mathbf{e}}_x)$ where $\underline{\mathbf{e}}_x$ is, as in the previous section, the machine direction of the outer liner.

The tangent elastic modulus E_{11} was measured for each sample. By considering classical orthotropic linear elastic stress–strain constitutive relations under plane stress assumptions, the experimentally measured E_{11} moduli can be expressed with respect to the elastic constants E_x, E_y, G_{xy} and ν_{yx} or ν_{xy} [13], which are respectively the machine direction elastic modulus, the cross-direction elastic modulus, the in-plane shear modulus, the in-plane Poisson's coefficient. Using this expression for E_{11}, the values of the elastic constants were determined by fitting the experimental data. The obtained values are shown in Table 1. It is worth noting that the determined elastic parameters reach values commonly encountered for paper materials [14,15].

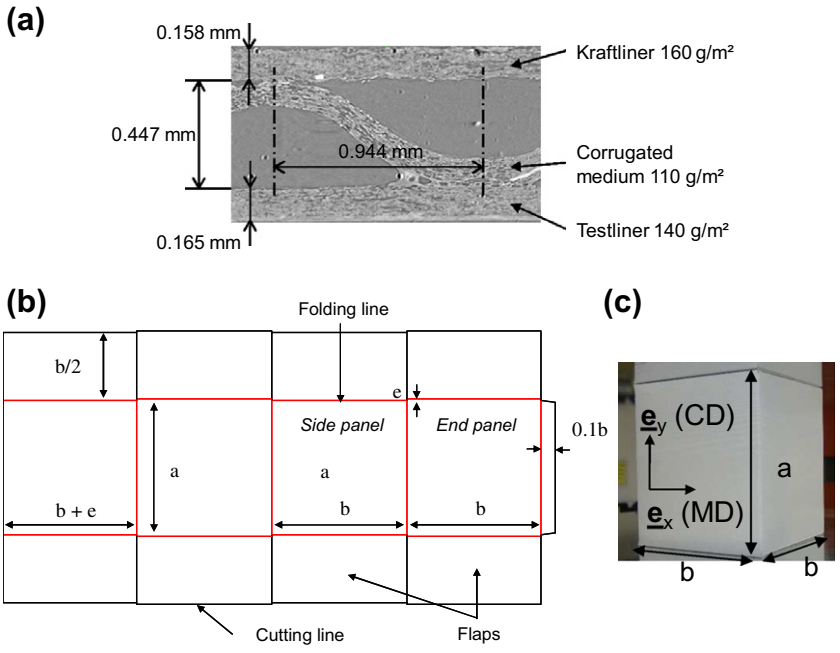

Fig. 1. (a) Picture of the cross-section of a G-flute profile corrugated board: image extracted from a 3D microtomography volume obtained at the European Synchrotron Radiation Facility (ESRF) on beamline ID19. (b) Box blank. (c) Assembled box and dimensions.

Table 1
In-plane elastic constants of the 160 g/m^2 outer kraftliner.

E_x (N/mm^2)	E_y (N/mm^2)	G_{xy} (N/mm^2)	ν_{xy}	ν_{yx}
6870	2154	2104	0.22	0.07

Table 2
Tsai–Wu criterion parameters.

X_t (N/mm^2)	X_c (N/mm^2)	Y_t (N/mm^2)	Y_c (N/mm^2)	S (N/mm^2)
35.5	−13.0	12.5	−7.0	14.0

To determine the yield point (or the elastic limit) the strategy consisted in identifying the deviation point where the experimental strain energy density deviates from the theoretical elastic strain energy. Then, the yield surface f was described using the Tsai–Wu equation for plane stress conditions to fit the experimental points:

$$f = \Gamma_1\sigma_{xx} + \Gamma_2\sigma_{yy} + \Gamma_{11}\sigma_{xx}^2 + \Gamma_{22}\sigma_{yy}^2 + \Gamma_{66}\sigma_{xy}^2 + 2\Gamma_{12}\sigma_{xx}\sigma_{yy} = 1, \tag{1}$$

where

$$\Gamma_{11} = -\frac{1}{X_tX_c}, \quad \Gamma_{22} = -\frac{1}{Y_tY_c}, \quad \Gamma_{12} = -\frac{1}{2\sqrt{X_tX_cY_tY_c}},$$
$$\Gamma_1 = \frac{1}{X_t} + \frac{1}{X_c}, \quad \Gamma_2 = \frac{1}{Y_t} + \frac{1}{Y_c}, \quad \Gamma_{66} = \frac{1}{S^2},$$

with σ_{xx}, σ_{yy} and σ_{xy}, the stress tensor components expressed in the material reference coordinate system $(\underline{\mathbf{e}}_x, \underline{\mathbf{e}}_y)$, X_t, X_c, Y_t, Y_c and S some parameters experimentally determined. These parameters are usually interpreted as follows: X_t is the tensile elastic limit along the $\underline{\mathbf{e}}_x$ direction, Y_t is the tensile elastic limit along the $\underline{\mathbf{e}}_y$ direction, X_c is the compressive elastic limit along the $\underline{\mathbf{e}}_x$ direction, Y_c is the compressive elastic limit along the $\underline{\mathbf{e}}_y$ direction and S is the shear elastic limit in the plane $(\underline{\mathbf{e}}_x, \underline{\mathbf{e}}_y)$. Their numerical values are given in Table 2. As it has been shown in some studies [17,16], the Tsai–Wu criterion is not optimum due to its quadratic form, which does not permit to accurately describe the complex shape of the actual yield surface of papers. Nevertheless, it permits to represent the difference between the tensile and compressive behaviour of paper and was adopted by several authors [18,19,3]. Here, it was considered accurate enough to determine where the outer liner reaches its elastic limit during the box compression (see Section 3.3).

2.3. Estimation of the residual stresses in the outer liner

One way to assess the residual stresses resulting from the corrugated board manufacturing operations is to machine away the outer liner [20]. Indeed, as the outer liner is removed, the board curvatures in both the $\underline{\mathbf{e}}_x$ and $\underline{\mathbf{e}}_y$ directions change in response to the unbalanced forces. It should be noted that no appreciable twist of the samples before and after the outer liner removing could be observed. Then, the residual stresses in the outer liner can be interpreted as the stresses which prevent the board from bending. The radii of curvature in the $\underline{\mathbf{e}}_x$ and $\underline{\mathbf{e}}_y$ directions of five samples of 15 mm wide and 150 mm long were measured before and after the outer kraftliner was removed. The radii of curvature were assessed using a millimetre paper placed underneath these strips. In order to calculate the residual stresses, the strip was considered as a elastic beam. Solving the equilibrium of forces and moments of a two layer beam, the residual stress σ_{ri} (along the MD $i = x$ and the CD $i = y$) in the outer liner can be expressed as follows [21]:

$$\sigma_{ri} = \left(\frac{1}{R_i} - \frac{1}{R_{0i}}\right)\frac{h_a^4E_{ai}^2 + 2E_{ai}E_{bi}h_ah_b\left(3h_ah_b + 2h_a^2 + 2h_b^2\right) + h_b^4E_{bi}^2}{6E_{ai}h_ah_b(h_a + h_b)}, \tag{2}$$

where E_{ai} and E_{bi} are the elastic moduli along the MD and CD of the board after the outer layer was removed and of the outer liner, respectively. h_a and h_b are the thicknesses the board after the outer layer was removed and of the outer liner, respectively. $1/R_{0i}$ and $1/R_i$ are the curvatures of the board after and before the outer liner was removed. As the corrugated board is perfectly flat, note that the curvatures $1/R_i$ were equal to zero in the two directions. E_{ai} was assessed in the MD and CD measuring the bending stiffnesses D_i of the board after the outer liner was removed. A two-point bending testing apparatus (Büchel – Van der Korput (Büchel BV, Utrecht, The Netherlands) Bending Tester (max. sensor force 5 N)) was used. Rectangular samples (38.1 × 69.9 mm^2) were cut along the machine and cross directions and tested according to the ISO2493 standard. Then, elastic moduli E_{ai} were estimated according to the theory of the single layer beam as follows:

$$E_{ai} = \frac{12D_i}{h_a^3}. \tag{3}$$

The elastic moduli E_{bi} is equal to E_x and E_y along the machine direction and the cross-direction, respectively. The outer liner has a thickness h_b = 0.16 mm (see also Fig. 1). Other values are given in Tables 1 and 3.

2.4. Box compression tests

Compression tests were performed with an Instron 5569 press at a compression velocity of 13 mm/min along the $\underline{\mathbf{e}}_{y'}$ direction (see Fig. 2a). The compression plates were made up of polished aluminium. A picture of a box, which was placed between the compression plates before the test, is shown in Fig. 2a. During these experiments, the compression force F and the axial plate displacement δ were recorded. This permitted to calculate the following macroscopic box axial stress Σ simply defined as

$$\Sigma = \frac{F}{S_0}, \tag{4}$$

where $S_0 = 4e(b - e)$ is defined arbitrarily as the surface of the box cross-section perpendicular to the compression axis $\underline{\mathbf{e}}_{y'}$. Similarly, a macroscopic strain ε is defined as

$$\varepsilon = \ln\frac{a + \delta}{a}. \tag{5}$$

A typical stress–strain curve obtained during a test is displayed in Fig. 2b.

2.5. Stereocorrelation technique

Two of the external panel surfaces were coated with a random pattern made of small black ink speckles. In order to estimate the 3D displacement field of these two surfaces, the stereocorrelation technique was performed using the DIC Software 7D® [22]. During the compression test, two images of the deforming panels and of their superimposed speckle patterns were recorded simultaneously and sequentially by using, for stereovision, two cameras (Nikon 200D, 3872 × 2592 pixels), whose relative position and orientation α were known. The setup is presented in Fig. 2c. The angle α was less than 5°. Fig. 2d depicts a typical pair of images taken by the left and the right cameras. Then, the correspondence between two image points belonging to the pair of simultaneously recorded images at the initial configuration (at t_0) were identified by applying a image correlation technique using square windows of 10 × 10

Table 3
Measurement of the residual stresses in the outer liner.

D_x (N m)	D_y (N m)	E_{a_x} (N/mm^2)	E_{a_y} (N/mm^2)	$1/R_{0x}$ (m^{-1})	$1/R_{0y}$ (m^{-1})	σ_{r_x} (N/mm^2)	σ_{r_y} (N/mm^2)
5.1×10^{-3}	20.8×10^{-3}	254	1048	0.75	2.44	−2.65	−2.53

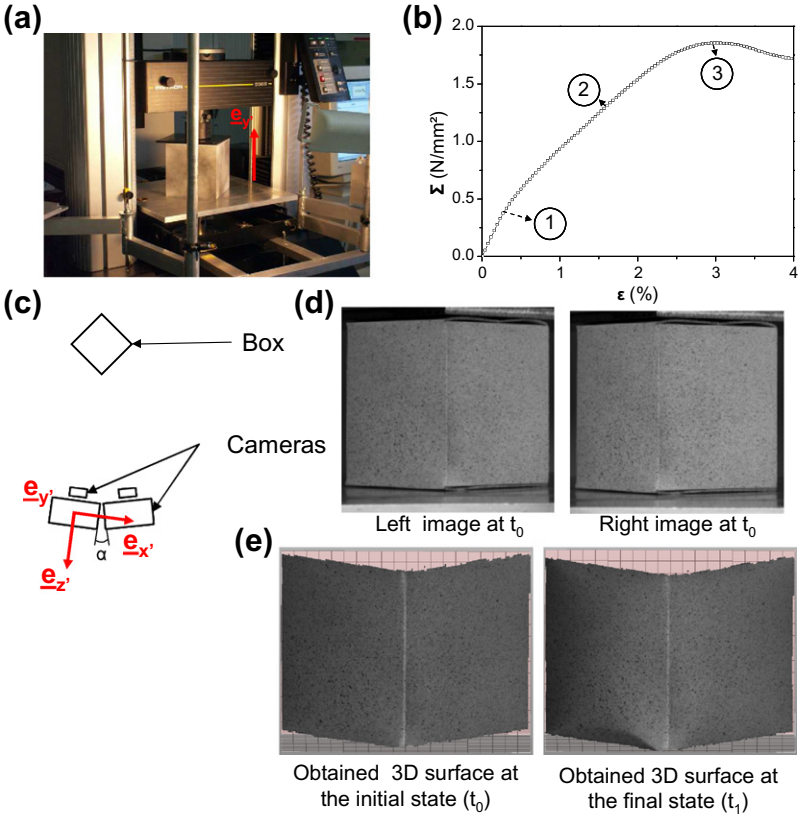

Fig. 2. (a) Picture of a box in the compression test set-up. (b) Typical experimental curve of the box compression stress with respect to the box compression strain. (c) Scheme of the imaging set-up. (d) Pictures of the box at the initial state (t_0). (e) Reconstructed 3D images of the surfaces of panels before the compression test (t_0) and during the compression test at the maximum recorded stress (final state t_1 corresponding to point no. 3 indicated in graph (b)).

pixels and subsets of 10 × 10 pixels centred around the corners of the windows. This stage requires the minimisation of a correlation function and involves to interpolate the grey levels using bilinear interpolation function of the left and right images. Then, the 3D coordinates x', y' and z', of a physical point were computed by triangulation. This allowed the surface of the studied panels to be reconstructed, as shown in the left image in Fig. 2e. Note that the surface at the horizontal edges could not be reconstructed. The correlation did not allow the reconstruction of a zone with a height of 2 mm close to the top horizontal edge and of a zone with a height of 3 mm close to the bottom horizontal edge. At each stage of the sequence, the principle of the surface reconstruction is similar, *i.e.* the left image taken at t_0 (see Fig. 2e) is used as reference image, which is correlated with the left and right images taken at each sequence (for instance the final configuration t_1 in Fig. 2e), respectively. This permits to build at each sequence step the surface in the current configuration. The error on this point location is mainly due to the precision of the correlation method. In this case, it can be estimated to be lower than 0.1 pixel.

Then, the 3D displacement field $\underline{\mathbf{u}}(x',y',z') = u'\underline{\mathbf{e}}_{x'} + v'\underline{\mathbf{e}}_{y'} + w'\underline{\mathbf{e}}_{z'}$ of all points of the panels was calculated by analysing a sequence of reconstructed surfaces. As an example, Fig. 3a shows the out-of-plane displacement w' of the surface of the two studied panels in the coordinate system of the left camera ($\underline{\mathbf{e}}'_x, \underline{\mathbf{e}}'_y, \underline{\mathbf{e}}'_z$). Finally, in this study, the displacement field was expressed in the panel local coordinate system ($\underline{\mathbf{e}}_x, \underline{\mathbf{e}}_y, \underline{\mathbf{e}}_z$), as shown in Fig. 3b. In this latter coordinate system, the 3D displacement field is written as $\underline{\mathbf{u}}(x,y,z) = u\underline{\mathbf{e}}_x + v\underline{\mathbf{e}}_y + w\underline{\mathbf{e}}_z$. For the calculation of the strain field, the displacement field was used in its raw form and in a smoothed form. The Matlab® smooth function, based on moving average, was applied along the $\underline{\mathbf{e}}_x$ and $\underline{\mathbf{e}}_y$ directions. Fig. 3c–f exhibit the smoothing effect on the w, u and v components respectively, for some lines along the $\underline{\mathbf{e}}_x$ direction. An example of the map of the w component after a smoothing operation is provided in Fig. 3d. It can be observed that the smoothing operation gives an accurate fit of this displacement component.

Thereafter, the components E_{xx}, E_{yy} and E_{xy} of the Green–Lagrange in-plane strain tensor $\underline{\underline{\mathbf{E}}}$ were estimated:

$$E_{xx} = \frac{\partial u}{\partial x} + \frac{1}{2}\left[\left(\frac{\partial u}{\partial x}\right)^2 + \left(\frac{\partial v}{\partial x}\right)^2 + \left(\frac{\partial w}{\partial x}\right)^2\right],$$
$$E_{yy} = \frac{\partial v}{\partial y} + \frac{1}{2}\left[\left(\frac{\partial u}{\partial y}\right)^2 + \left(\frac{\partial v}{\partial y}\right)^2 + \left(\frac{\partial w}{\partial y}\right)^2\right],$$
$$2E_{xy} = \frac{\partial u}{\partial y} + \frac{\partial v}{\partial x} + \frac{\partial u}{\partial x}\frac{\partial u}{\partial y} + \frac{\partial v}{\partial x}\frac{\partial v}{\partial y} + \frac{\partial w}{\partial x}\frac{\partial w}{\partial y}. \quad (6)$$

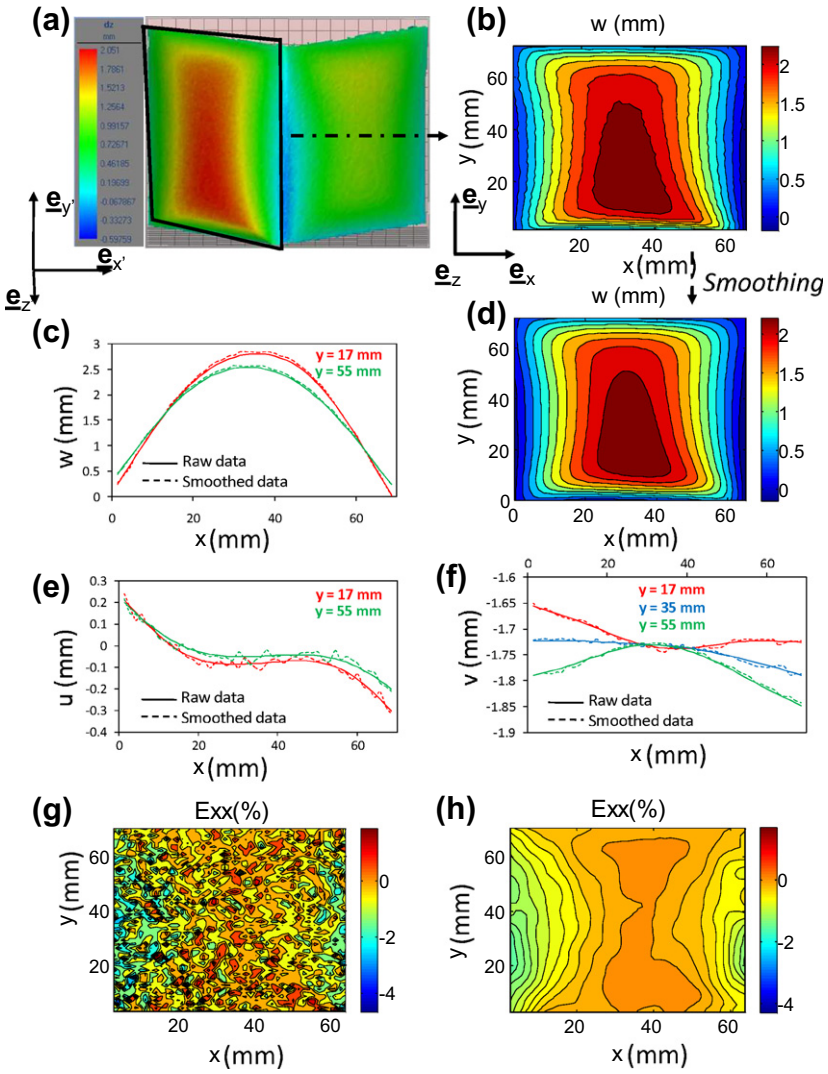

Fig. 3. (a) Component w' of the displacement field of the two studied panels in the (x',y',z') coordinate system. (b) Displacement w of the panel with outer flaps (see the arrow) in the panel coordinate system (x,y,z). (c) Smoothing effect on the displacement component w at $y = 17$ mm and $y = 55$ mm. (d) Displacement w after a smoothing operation (see the arrow). (e) Smoothing effect on the displacement component u at $y = 17$ mm and $y = 55$ mm. (f) Smoothing effect on the displacement component v at $y = 17$ mm, $y = 35$ mm and $y = 55$ mm. (g) Component E_{xx} of the strain field (obtained from the raw displacement field). (g) Same component when the displacement field is smoothed. Here, the reference configuration for the field measurements is the configuration of the box after its manufacturing.

The above spatial partial derivatives were calculated by using a standard centred finite difference scheme. Fig. 3g reveals that the component E_{xx} obtained using the raw displacement field is largely heterogeneous. It is worth noting that the smoothed displacement field allows a less "noisy" strain field to be obtained at the macroscopic scale. The information contained in the smooth displacement field appeared us to be satisfactory for the rest of the analysis.

3. Results

In this section, the behaviour of a panel with outer flaps of a cubic box with dimensions $73 \times 73 \times 73$ mm^3 is treated.

3.1. Initial displacement and strain fields resulting from the box manufacturing

After the box manufacturing operations, it appeared that the panels were not perfectly flat. Indeed, an out-of-plane displacement w_0 could be revealed thanks to the reconstructed 3D surface at the initial state t_0 obtained by the stereocorrelation technique, (see Fig. 2e). Fig. 4 reveals this component for the panel with outer flaps which is treated in this section. The w_0 component reaches its maximum value at the centre of the panel whereas it is zero along the vertical edges. As the panel was not totally reconstructed, a slight out-of-plane displacement is noticed close to the bottom and top horizontal edges of the map. The displacement components u_0 and v_0 resulting from the box manufacturing were

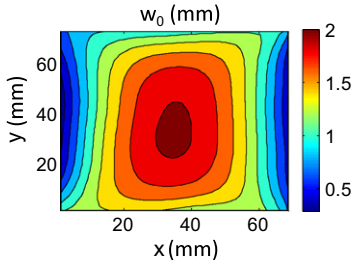

Fig. 4. Map of the initial out-of-plane component w_0 due to box manufacturing operations for a box panel with outer flaps (box dimensions $73 \times 73 \times 73$ mm^3).

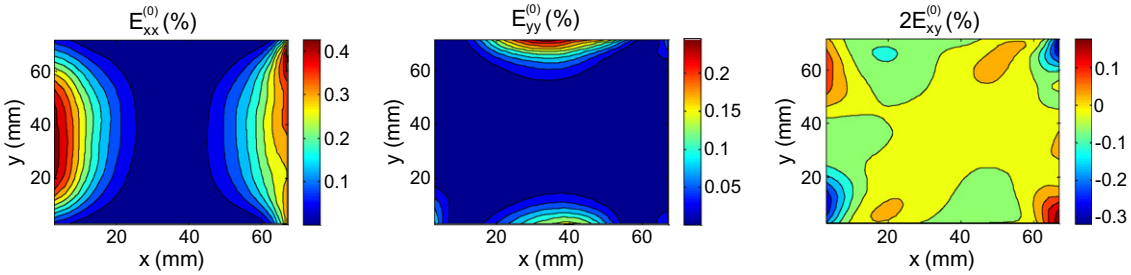

Fig. 5. Maps of the components of the initial strain field $\underline{\underline{\mathbf{E}}}^{(0)}$ due to box manufacturing operations on the surface of the panel with outer flaps (box dimensions $73 \times 73 \times 73\ mm^3$).

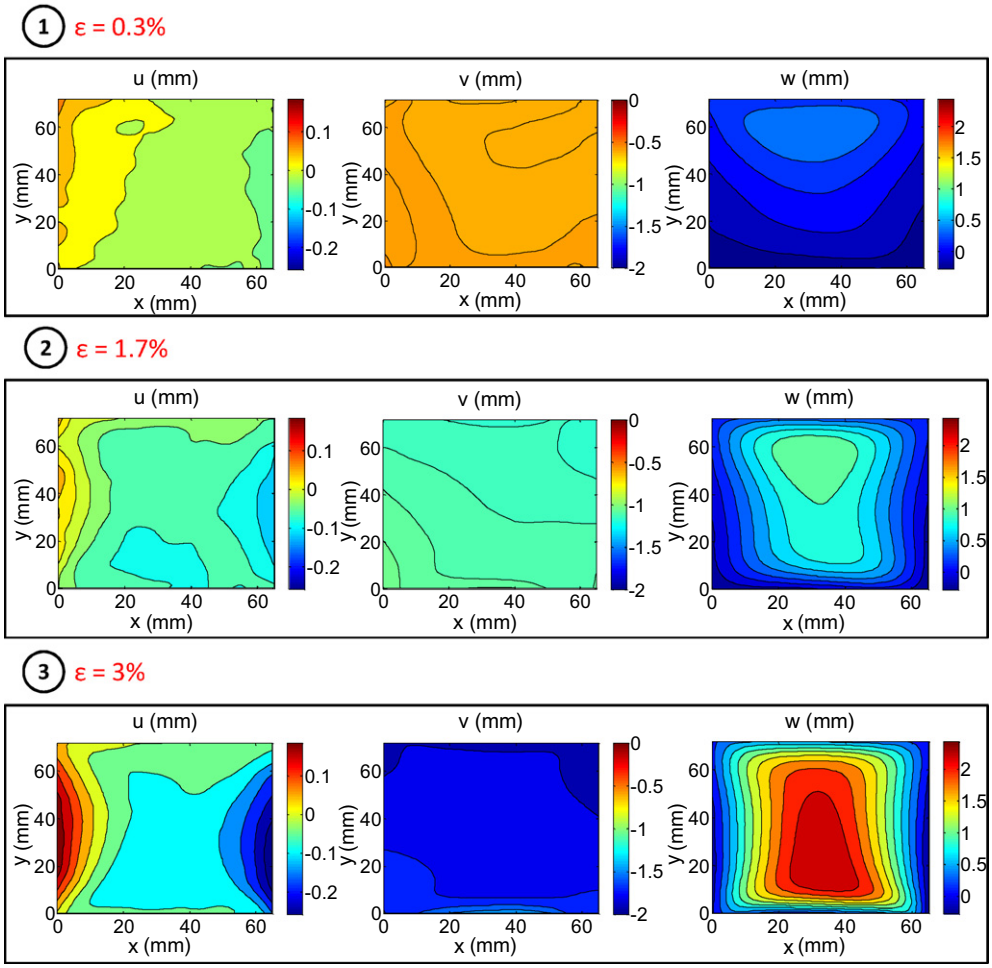

Fig. 6. Maps of the components u, v and w of the displacement field at three compression stages noted 1, 2 and 3 corresponding to macroscopic compression strains $\varepsilon = 0.3\%$, 1.7% and 3%, respectively (see Fig. 2b). Here, the reference configuration for the field measurements is the configuration of the box after its manufacturing as in Fig. 3.

considered insignificant. Then, the three components of the related initial strain field noted $\underline{\underline{\mathbf{E}}}^{(0)}$ were assessed from Eq. (6). Fig. 5 depicts these components. The component $E_{xx}^{(0)}$ is different from zero only along the vertical edges where it reaches a maximum of 0.4% at the middle. The component $E_{yy}^{(0)}$ is maximum along the horizontal edges and reaches values twice lower. Notice that these components are positive, which is characteristic of a tensile deformation state. Finally, the component $E_{xy}^{(0)}$ is only significant in the corner regions (around 0.2%).

3.2. Displacement and strain fields resulting from the box compression

In this section, only the displacement and strain fields, which result from the box compression, are studied. The initial or reference configuration is the configuration of the box after its manufacturing.

3.2.1. Evolution of the displacement field during compression

The stereocorrelation technique was used to describe the displacement field of the panel at three compression stages, corresponding to the following box macroscopic strains $\varepsilon = 0.3\%$, 1.7% and 3%, respectively. The corresponding stress–strain curve is that given in Fig. 2b. As shown in this figure, the last compression strain $\varepsilon = 3\%$ corresponds to the box compression critical strain.

The components u, v and w of the displacement field are displayed in Fig. 6. Firstly, it is worth noting that the displacement components are largely heterogeneous whatever the compression strain. The out-of-plane displacement w and the in-plane

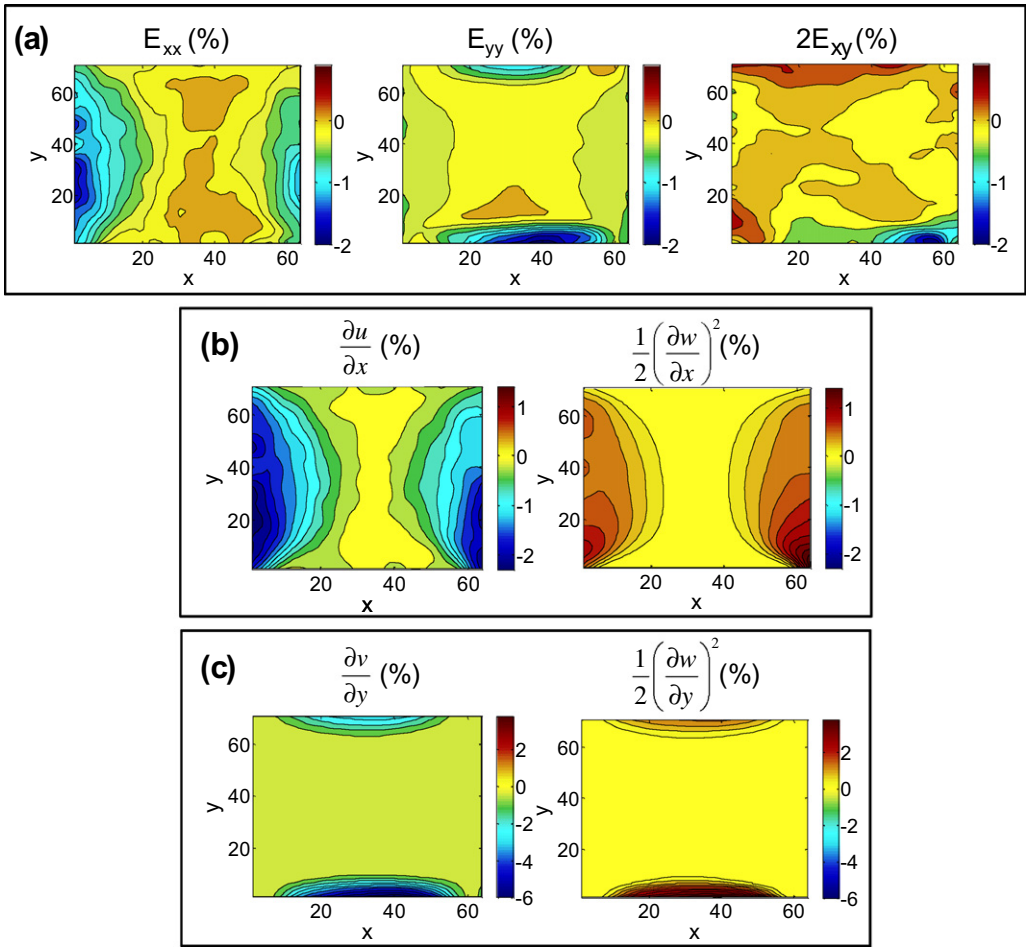

Fig. 7. (a) Components of the Green–Lagrange strain tensor of the panel with outer flaps at the critical strain ε_{max} = 3%, box dimensions 73 × 73 × 73 mm^3. (b) Maps of the horizontal in-plane displacement gradient and out-of-plane displacement gradient contributing to the strain component E_{xx}. (c) Same maps for the strain component E_{yy}. Here, the reference configuration for the field measurements is the configuration of the box after its manufacturing.

displacement v are of the same order of magnitude and these two components are largely higher than the in-plane displacement u.

The out-of-plane displacement component w is never equal to zero, even for the first compression stage, *i.e.* ε = 0.3%. This clearly indicates that the panel buckling is the predominant phenomenon and that it occurs and develops very early during the box compression. It is also interesting to notice that this field is not symmetric with respect to the horizontal median line of the panel. The maximum values of this component are obtained for a zone, located close to the top horizontal edge at the beginning of the compression, which is moved towards the bottom edge of the box at the critical strain, *i.e.* ε = 3%. Besides, the surface of the zone was increased during the compression, as the values of w close to the box edges remained nearly equal to zero or were even slightly negative. Thus, high gradients for this component were found when going through the panel from its edges to the previous central zone, especially along the $\underline{\mathbf{e}}_y$ direction.

The component v of this displacement field was found to be of the same order as w. But quite astonishingly, it can also be observed that this component is nearly homogeneous over the whole panel surface. This means that the panel exhibits a vertical translatory motion during the box compression. Its origin might be related to a motion and a compression of the outer flaps joined to the panel, and more presumably to the crush of the junction scores during the compression experiment. Unfortunately, the scores are outside the correlation images. This point could be improved in future works.

The component u of the displacement field was observed to be small compared to v and w. It is nevertheless interesting to analyse it more precisely, especially for the last compression stage. It makes indeed appear that there are zones in the centre of the panel and close to its corners, where this component is very weak. On the contrary, along the vertical edges of the panel, this component is completely heterogeneous and shows a maximum approximately located at the median height of the panel. Thus, during the box compression, the vertical edges of the panel do not remain straight and tend to move towards the panel centre as the compression strain increases.

3.2.2. Strain field at the critical strain and contributions of the displacement components

When calculating the components of the Green–Lagrange strain tensor, it appeared that the contribution of some spatial gradients of u, v and w are insignificant (<0.0015). This permits to write the strain components E_{xx}, E_{yy} and $2E_{xy}$ adopting the following reduced expressions, which correspond to a von Kármán-type strain field [13]:

$$\begin{aligned} E_{xx} &\approx \frac{\partial u}{\partial x} + \frac{1}{2}\left(\frac{\partial w}{\partial x}\right)^2, \\ E_{yy} &\approx \frac{\partial v}{\partial y} + \frac{1}{2}\left(\frac{\partial w}{\partial y}\right)^2, \\ 2E_{xy} &\approx \frac{\partial u}{\partial y} + \frac{\partial v}{\partial x} + \frac{\partial w}{\partial x}\frac{\partial w}{\partial y}. \end{aligned} \tag{7}$$

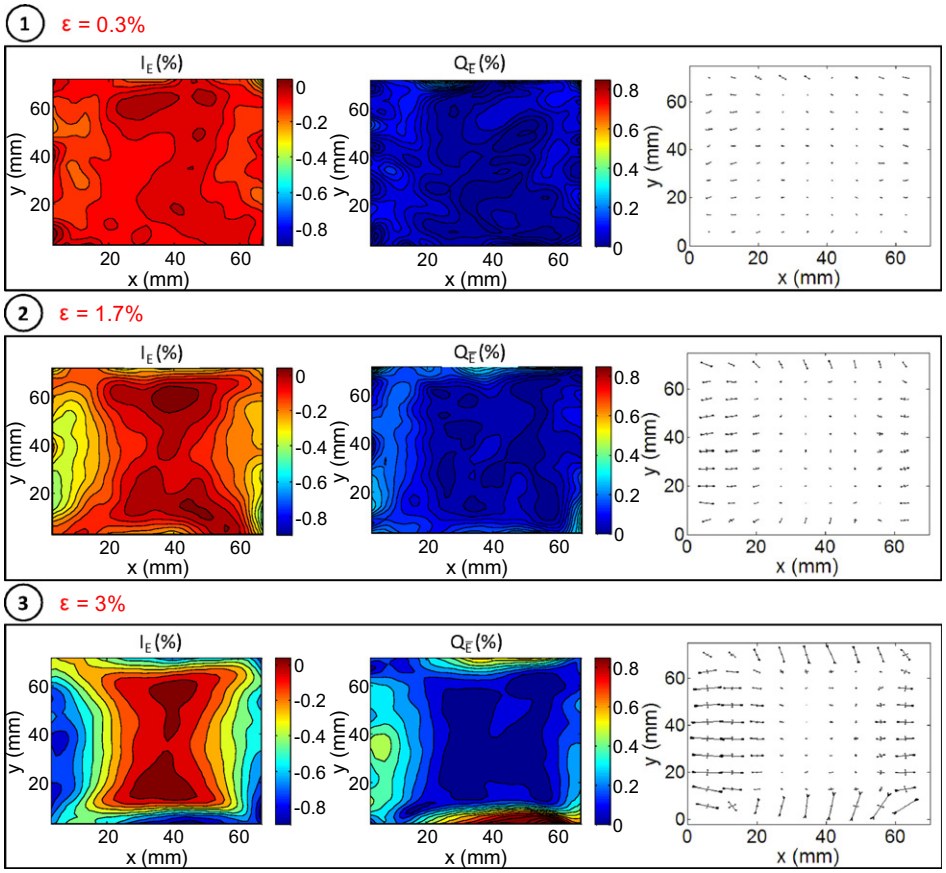

Fig. 8. Maps of the invariants of the strain tensor I_E and $Q_{\bar{E}}$, and map showing the magnitude and the orientation of the principal strain components at three compression stages $\varepsilon = 0.3\%$, $\varepsilon = 1.7\%$ and $\varepsilon = 3\%$ for the panel with outer flaps of the box with dimensions $73 \times 73 \times 73$ mm^3. Here, the reference configuration for the field measurements is the configuration of the box after its manufacturing.

Fig. 7a exemplifies the components E_{xx}, E_{yy} and $2E_{xy}$ of the strain field at the critical compression strain $\varepsilon = 3\%$. This stage of the compression was chosen because this is *a priori* the most deformed strain stage. Fig. 7b and c reveal the contributions of the gradient of the in-plane u and v displacements $\partial u/\partial x$ and $\partial v/\partial y$, and of the gradient of the out-of-plane w displacement $1/2(\partial w/\partial x)^2$ and $1/2(\partial w/\partial y)^2$ to the strains E_{xx} and E_{yy}. This latter contribution has positive values, whereas the in-plane ones are negative. However, the out-of-plane contribution only reaches 50% at the maximum of the in-plane contribution. Of course, it cannot be neglected and emphasises the significant influence of the panel buckling on the strain state. But the in-plane contribution is predominant, and this explains why there are rather narrow zones in tension at the surface of this panel despite its pronounced bulging due to the box compression.

As revealed in Fig. 7a, the values of the strain components are almost equal to zero in the region of the panel centre. By contrast the strain variations are more pronounced along the panel edges. Noticeable variations of E_{xx} can be observed along the vertical edges of the box, whereas the variations of E_{yy} appear mainly along the horizontal edges of the panel. The negative values of these strain components are characteristic of a compressive deformation state. The maximum compressive strains are attained at the middle of the edges, and gradually decrease close to the corner regions. It is also interesting to notice that the highly compressed zones (E_{xx} or $E_{yy} \leqslant -1\%$) are wider along the vertical edges than along the horizontal edges, despite these latter edges are perpendicular to the box compression axis. The relatively limited intensity of the component E_{yy} over the whole surface of the outer liner may certainly be related to strong phenomena of compression of the flaps and crush of the horizontal scores, which consequently "reduce" the deformation of the outer liner of the panel in the vertical direction. The high intensity of the component E_{xx} is more surprising. It reveals the complexity of the deformation mechanisms of the box. It shows also that the deformation of the observed panel is severely constrained by its neighbouring panels.

3.2.3. Evolution of the strain field during compression

In the following,, the principal components E_I, E_{II} of the in-plane strain tensor $\underline{\underline{\mathbf{E}}}$ and the principal direction angle β measured from the principal material coordinate system $(\underline{\mathbf{e}}_x, \underline{\mathbf{e}}_y)$ to the principal strain coordinate system $(\underline{\mathbf{e}}_I, \underline{\mathbf{e}}_{II})$ were calculated as

$$E_I = \left(\frac{E_{xx}+E_{yy}}{2}\right) + \frac{1}{2}\sqrt{(E_{xx}-E_{yy})^2 + (2E_{xy})^2}, \tag{8}$$

$$E_{II} = \left(\frac{E_{xx}+E_{yy}}{2}\right) - \frac{1}{2}\sqrt{(E_{xx}-E_{yy})^2 + (2E_{xy})^2}, \tag{9}$$

$$\beta = \frac{1}{2}\arctan\left(\frac{2E_{xy}}{E_{xx}-E_{yy}}\right). \tag{10}$$

To better describe the strain state and its evolution during the box compression, the first in-plane strain invariant I_E, which accounts for the mean compressive or tensile strain, and the in-plane strain invariant $Q_{\bar{E}}$, which accounts for the mean shear strain, were determined by using the following expressions:

$$I_E = \frac{1}{2}Tr(\underline{\underline{\mathbf{E}}}) = \frac{E_I + E_{II}}{2},$$

$$Q_{\bar{E}} = \sqrt{\frac{1}{2}Tr\left(\underline{\underline{\bar{\mathbf{E}}}} \cdot \underline{\underline{\bar{\mathbf{E}}}}\right)} = \frac{|E_I - E_{II}|}{2}, \tag{11}$$

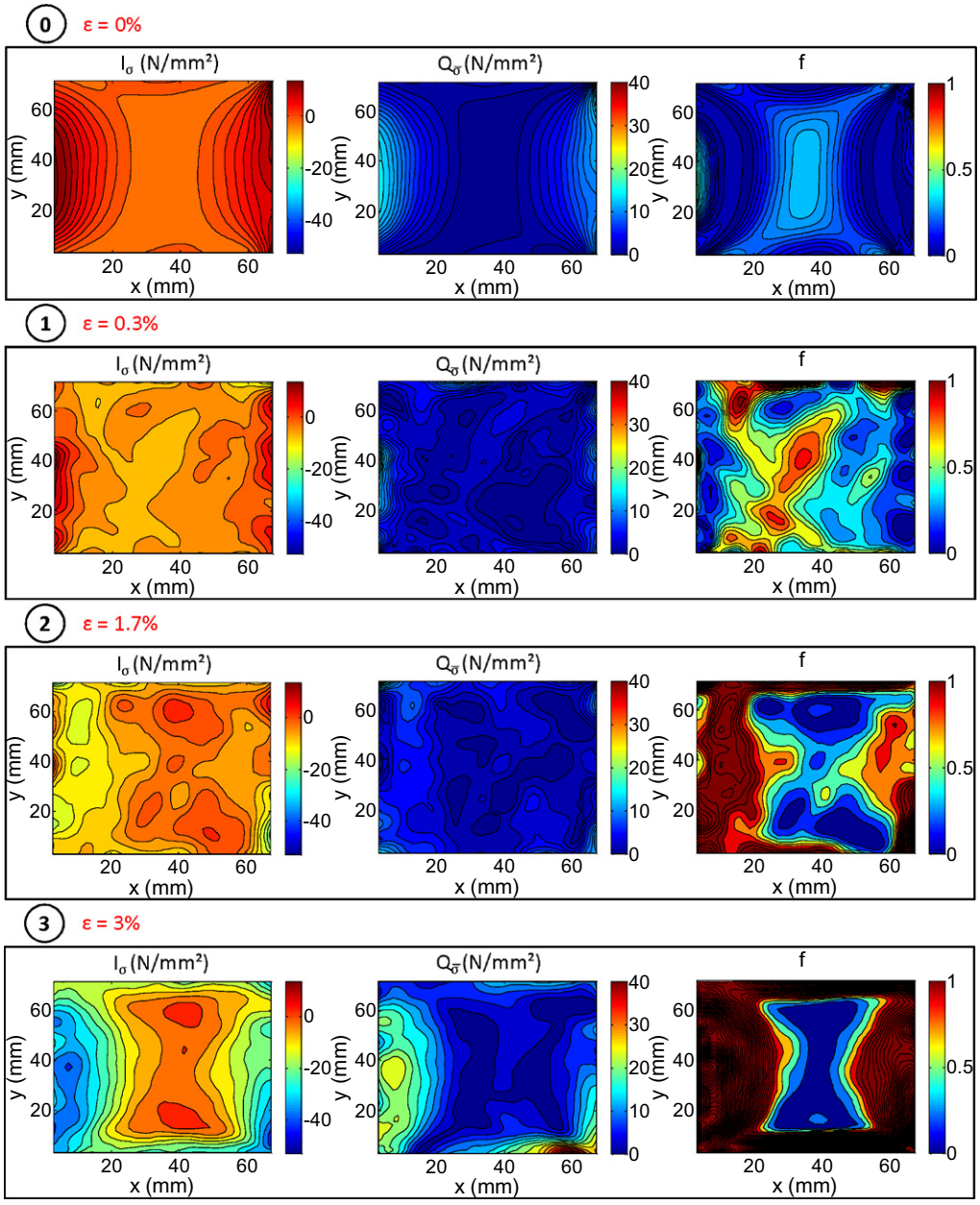

Fig. 9. Maps of the invariants of the stress tensor I_σ and $Q_{\bar{\sigma}}$, and map of the yield criterion before the compression $\varepsilon = 0\%$ and at three compression stages $\varepsilon = 0.3\%$, $\varepsilon = 1.7\%$ and $\varepsilon = 3\%$ for the panel with outer flaps of the box with dimensions $73 \times 73 \times 73$ mm^3.

where $\underline{\underline{\mathbf{E}}} = \underline{\underline{\mathbf{E}}} - \frac{1}{2} Tr(\underline{\underline{\mathbf{E}}})\underline{\underline{\mathbf{I}}}$ is the deviatoric part of the strain tensor, $\underline{\underline{\mathbf{I}}}$ is the identity tensor and Tr is the trace operator.

Fig. 8 depicts the maps of the invariants I_E and $Q_{\bar{E}}$ for three compression stages. For each couple of maps, a third map shows the magnitude and the orientation of the principal strains E_I and E_{II} in some points of the panel. Considering the evolution of I_E and $Q_{\bar{E}}$ during box compression, one can notice that the regions along the vertical and horizontal edges, which have been identified previously as the most deformed zones, at the last compression stage, behave very differently. The compressive and shear states gradually increase in magnitude along the vertical edges during the compression, *i.e.* from $\varepsilon = 0.3\%$ up to 3%, whereas they increase suddenly at the last compression stage along the horizontal edges. At this stage, along the vertical edges, the mean compressive strain is twice greater than the mean shear strain, whereas, along the horizontal edges, values are equivalent. This phenomenon is well illustrated in the maps showing the magnitude of the principal strains. In addition, there is a large zone around the panel centre, where the strain state does not evolve significantly during compression.

Finally, the compression leads to different variations of the strain state at the panel scale. On the one hand, the buckling phenomenon results in a regular increase of the strain state along the vertical edges. On the other hand, it leads to a sudden increase of the strain state along the horizontal edges at the critical box compression strain. The last phenomenon can be related to the occurrence of a crease close to the bottom edge, revealed in Fig. 2e.

3.3. Stress field in the outer liner

It was assumed that the full stress field $\underline{\underline{\boldsymbol{\sigma}}}$ in the outer liner was decomposed into three contributions: one resulting from the residual stress field induced by the board manufacturing operation $\underline{\underline{\boldsymbol{\sigma}}}_r$, one other resulting from the box manufacturing operation $\underline{\underline{\boldsymbol{\sigma}}}_0$ and one other resulting from the box compression $\underline{\underline{\boldsymbol{\sigma}}}_e$:

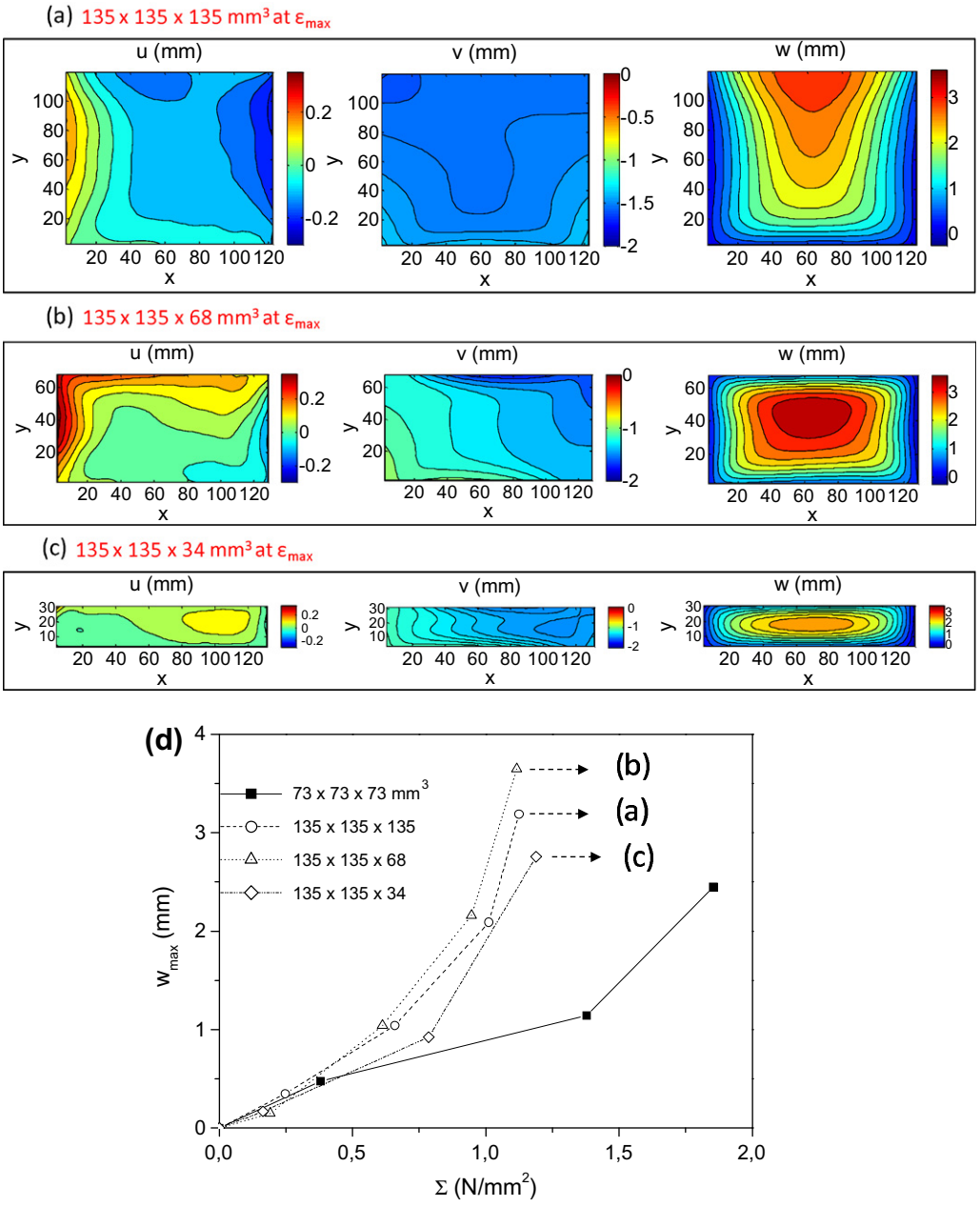

Fig. 10. Maps of the components of the displacement fields of the panels with outer flaps at the critical strain $\varepsilon = 3\%$, for the box with dimensions $135 \times 135 \times 135$ mm^3. (b) Same maps for the box with dimensions $135 \times 135 \times 68$ mm^3. (c) Same maps for the box with dimensions $135 \times 135 \times 34$ mm^3. (d) Maximum out-of-plane displacement w_{max} evolution with respect to the compression stress. Here, the reference configuration for the field measurements is the configuration of the box after its manufacturing.

$$\underline{\underline{\boldsymbol{\sigma}}} = \underline{\underline{\boldsymbol{\sigma}}}_e + \underline{\underline{\boldsymbol{\sigma}}}_0 + \underline{\underline{\boldsymbol{\sigma}}}_r. \tag{12}$$

To evaluate these stress fields, the previously determined parameters of the orthotropic linear elastic model (see Section 2.2) were used as well as the measured strain fields and the residual stress components measured in Section 2.3. Thereafter, the three components σ_{xx}, σ_{yy} and σ_{xy} of the stress field were determined. Here, it was assumed that plane stress conditions hold for the outer liner. The first invariant I_σ which accounts for the mean compressive or tensile stress and the invariant $Q_{\bar{\sigma}}$ which accounts for the mean shear stress were also calculated as follows:

$$I_\sigma = \frac{\sigma_I + \sigma_{II}}{2}.$$
$$Q_{\bar{\sigma}} = \frac{|\sigma_I - \sigma_{II}|}{2}. \tag{13}$$

Fig. 9 shows maps of I_σ and $Q_{\bar{\sigma}}$ at four compression stages $\varepsilon = 0\%$, $\varepsilon = 0.3\%$, $\varepsilon = 1.7\%$ and $\varepsilon = 3\%$. For each couple of the maps of stress invariants, the map of the values of the yield Tsai–Wu criterion f, established in Section 2.2, is shown in order to determine where the outer liner reaches its elastic limit in the panel ($f = 1$) and the corresponding compression stage. Before the compression (*e.g.* at $\varepsilon = 0\%$), one can observe significant tensile and shear states in the outer liner along the vertical edges which result from the board and box manufacturing. Elsewhere in the panel, the mean normal and shear stresses are weak. As the stress state is mostly an equibiaxial stress state (see I_σ at $\varepsilon = 0\%$), the values of the yield criterion remain largely lower than the yield limit ($f < 1$). At the first stage of the compression ($\varepsilon = 0.3\%$), the mean normal and shear stresses decrease along the vertical edges, whereas slight compressive and shear states are noticed in zones close to the

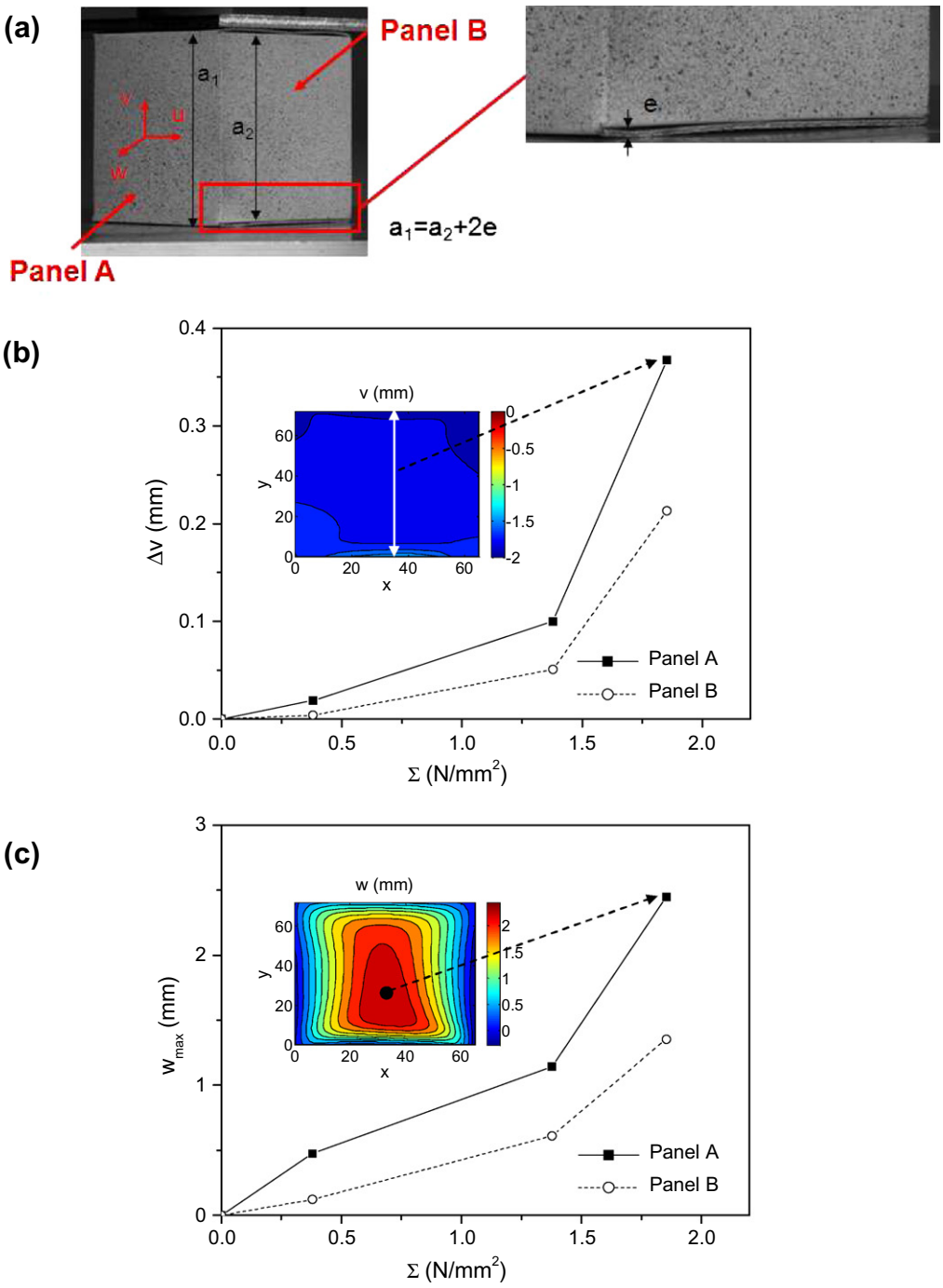

Fig. 11. (a) Pictures showing the difference of height between the panel with outer flaps (panel A) and the panel with inner flaps (panel B) for the box with dimensions $73 \times 73 \times 73$ mm^3. (b) Height reduction Δv versus box compression stress for both panels. (c) Maximum out-of-plane displacement w_{max} for both panels. Here, the reference configuration for the field measurements is the configuration of the box after its manufacturing.

panel centre. Then, the yield criterion show significant values in these regions. However, the elastic limit is not exceeded. This compression stage can be seen as an intermediate state where the contribution of the stresses resulting from residual stresses and box manufacturing induced stresses and the contribution of the elastic stresses resulting from the compression tend to cancel each other out. At the second compression stage ($\varepsilon = 1.7\%$), the elastic limit is reached ($f \geqslant 1$) along the vertical edges in quite large zones. Along the horizontal edges, the elastic limit is exceeded only in a narrow zone, which is characteristic of the beginning of the crush of the junction scores. At the last compression stage ($\varepsilon = 3\%$), the elastic limit is exceeded in more than one half of the total surface of the outer liner. Only the region around the panel centre is unaffected. Of course, as the model is only linear elastic, in the region where the elastic limit is exceeded, values of the components of the stress field are certainly overestimated.

In conclusion, the initial out-of-plane displacement due to the box manufacturing leads to an initial equibiaxial stress field in the outer liner, which permits to annihilate the compressive stress field resulting from the compression at the beginning of the box loading. In addition, the elastic limit is first reached along the vertical edges at the mid-compression stage.

4. Discussion

4.1. Influence of the box geometry

In order to study accurately the influences of the aspect ratio a/b on the one hand and panel dimensions on the other hand, three more boxes with different dimensions were tested. Boxes had bases of 135×135 mm^2 and heights $a = 135$, 68 and 34 mm (*i.e.* aspect ratios of panels $a/b = 1$, 0.5 and 0.25, respectively). For each box, the displacement field is described for one panel with outer flaps at the critical compression strain. The components u, v and w of the displacement fields are displayed in Fig. 10 for the three panels.

Comparing Figs. 10a–c and 6, the maps of the components of the displacement field differ essentially in magnitude. The maximum of the u component in the panel with a height of 135 mm is twice lower than the maximum recorded value in the panel with a height of 68 mm, which is in the same order of magnitude as in the panel previously described of 73×73 mm^2. On the contrary, the component u of the panel with a height of 34 mm remains close to zero along the vertical edges. The maximum of the w component is the highest in the panel with a height of 68 mm. It is only slightly lower for the panel with a height of 135 mm and significantly lower for the two other panels. As a result, the magnitudes of the displacement components seem to be clearly dependent on the aspect ratio and dimensions of the panel.

In order to better study this dependence, the evolution of the maximum recorded out-of-plane displacement w_{max} for the four types of panels with respect to the compression stress Σ up to its critical value is depicted in Fig. 10d. For panels with a length $b = 135$ mm, curves show a quite similar evolution. The gradient of w_{max} is becoming higher as the critical stress is being reached. The highest values of the out-of-plane component w are reached for the rectangular panel with an aspect ratio $a/b \approx 0.5$ and correspond to the lowest compression stresses. For the panel of 73×73 mm^2, the out-of-plane maximum values are largely lower and the related compression stresses are largely greater. Some of these observations (*e.g.* the highest load reached during compression for the panels with a length b of 73 mm compared with those having a length of 135 mm) can be explained by the very simplified assumptions based on elastic buckling theory adopted by McKee et al. [4] or Urbanik [5] to predict the compression strength of corrugated board boxes. Nonetheless, the slight differences observed between the behaviour of the various panels with a length $b = 135$ mm cannot be explained by these simplified theories. This shows that some improvement of these modelling approaches should be undertaken, as previously discussed by Viguié et al. [23]. This should be done for panels with outer flaps as well as for panels with inner flaps as shown in the next section.

4.2. Influence of panels' flaps

Fig. 11 allows a comparison between the behaviour of the panel with outer flaps and the panel with inner flaps (box with dimensions $73 \times 73 \times 73$ mm^3). Their geometry can be compared in Fig. 11a. Fig. 11b and c give the change of v noted Δv, defined as the positive difference between the vertical v displacements of the bottom and top horizontal edges, and the maximum recorded out-of-plane displacement w_{max}, with respect to the compression stress Σ up to its critical value. For the two kinds of panels, these parameters exhibit a smooth increase with the stress, followed by a sharp increase. However, the values of Δv and w_{max} obtained for the panel with inner flaps are systematically 30% or 40%, respectively, lower than those of the panel with outer flaps. This reveals that the buckling phenomenon of panels is heterogeneous at the box scale. The origin of this different behaviour between both types of panels can be attributed to their differences in geometry. The panel with inner flaps is indeed a little bit shorter than the panel with outer flaps (see Fig. 11a). As a consequence, it can be assumed that the panels with inner and outer flaps are not subjected to the same load at the same compression stage. Indeed, as the outer flaps have a low resistance in compression in the thickness direction, one can assume that the compression of the panel with inner flaps begins after the outer flaps have been compressed. This assumption can be confirmed by the value of Δv, at the first compression stage, which is almost zero for the panel with inner flaps. In numerous empirical and numerical models used for predicting the box compression behaviour, the compression load is considered equally distributed on the four panels. In the case of boxes with flaps, this assumption might lead to erroneous results. It can be assumed that the distribution of the load on the panels is constantly changing during the compression. In order to verify this assumption, the resulting forces and moments could be calculated in all panel sections. But this necessitates to know the full mechanical behaviour of all the components of the corrugated board.

4.3. Optimization of the mechanical behaviour of the outer liner

The stereocorrelation method gives interesting information on the heterogeneity of the strain and stress fields. There are zones which are more stressed in compression than others. During the beginning stages of the box compression, these zones are located in the vicinity of the vertical edges of the panels where the elastic limit can be exceeded quite soon. Thus, they could be reinforced in order to delay the buckling development. Later during box compression, it can be observed that the outer liner collapses in narrow zones close to the horizontal edges. Here again these zones could be reinforced. Besides, this observation suggests to reconsider the fact that the cross-direction of the corrugated board is systematically aligned along the direction of the compression loading.

One can also notice that the residual stresses in the outer liner induce a loss of mechanical performance of the outer liner in buckling situation. It could be interesting to adjust the residual stresses in the outer liner during the corrugated board manufacturing.

Optimized flap geometries or optimized folding line geometries could permit to get box panels with the same height, and thus more homogeneous and efficient distribution of the load on the four panels of the box.

5. Conclusion

A 3D DIC method was used and tailored to analyse the buckling behaviour of panels of corrugated board boxes during their compression. This technique is highly efficient to provide relevant data on the 3D displacement and strain fields in the outer liner of the box panels. Using a linear orthotropic constitutive law as well as a residual stress state analysis for the outer liner, the stress field could be also estimated. Highly compressed zones are first seen along the vertical edges where the elastic limit of the outer liner is exceeded quite soon during the box compression. Zones with a similar compressive strain state appear later along the horizontal edges. The critical measured stress for the box during compression is related to the collapse of these zones. The stereocorrelation technique gives some interesting information for modelling approaches. Firstly, von Kármán kinematic assumptions appear to be reasonably well suited. Secondly, as the elastic limit of the outer liner is exceeded early, numerical models aiming at describing the crush of boxes should preferably account for the elastic plastic behaviour or damage behaviour of the paper constituents of corrugated board. This approach gives also the real boundary conditions

the outer liner of the panels is subjected to. Depending on the observed panel, boundary conditions can change drastically. In future work, these data could be used to improve buckling and post-buckling prediction models of board panels made up of corrugated board. Real measured boundary conditions could also be used in numerical simulation aiming at describing these deformation phenomena.

Acknowledgements

Papeterie de Gondardennes (Gondardennes, France) are gratefully acknowledged for supplying G-flute corrugated boards. The authors acknowledge the European Synchrotron Radiation Facility (ESRF, Grenoble, France) long-term project "Heterogeneous Fibrous Materials" for giving them the opportunity to work on the ID19 beamline.

References

[1] Patel P, Nordstrand T, Carlsson LA. Local buckling and collapse of corrugated board under biaxial stress. Compos Struct 1997;39(1–2):93–110.
[2] Allansson A, Svard B. Stability and collapse of corrugated board; numerical and experimental analysis. Master's Thesis. Division of Structural Mechanics, LTH, Lund University, Lund, Sweden; 2001.
[3] Nordstrand T. Analysis and testing of corrugated board panels into the post-buckling regime. Compos Struct 2004;63:189–99.
[4] McKee RC, Gander JW, Wachuta JR. Compression strength formula for corrugated board. Paperboard Packag 1963;48(8):149–59.
[5] Urbanik TJ. Review of buckling mode and geometry effects on postbuckling strength of corrugated containers. Develop Validat Appl Inelastic Method Struct Anal Des 1996;343:85–94.
[6] Beldie L, Sandberg G, Sandberg L. Paperboard packages exposed to static loads – finite element modelling and experiments. Packag Technol Sci 2001;15:1–8.
[7] Biancolini ME, Brutti C. Numerical and experimental investigation of the strength of corrugated board packages. Packag Technol Sci 2003;16:47–60.
[8] Thorpe JL, Choi D. Corrugated container failure part 2 – strain measurements in laboratory compression tests. Tappi J 1992;75(7):155–61.
[9] Considine JM, Scott CT, Gleisner R, Zhu JY. Use of digital image correlation to study the local deformation field of paper and paperboard. In: 13th Fundamental research symposium, Cambridge; 2005.
[10] Meunier L, Chagnon G, Favier D, Orgéas L, Vacher P. Mechanical experimental characterisation and numerical modelling of an unfilled silicone rubber. Polym Test 2008;27:765–77.
[11] Orteu JJ. 3-D computer vision in experimental mechanics. Opt Laser Eng 2009;47:282–91.
[12] Viguié J. Comportements mécanique et hygroexpansif des matériaux lignocellulosiques pour l'emballage rigide – mechanical and hygroexpansive behaviour of lignocellulosic materials for rigid packaging. PhD thesis. Institut polytechnique de Grenoble (Grenoble INP), Grenoble, France; 2010.
[13] Reddy J. Mechanics of laminated composite plates and shells theory and analysis. second ed. Boca Raton (FL, USA): CRC Press LCC Publishing; 2000.
[14] Niskanen K, Kärenlampi P. In-plane tensile properties. Papermaking science and technology, Book 16, Paper Physics, Fapet Oy, Helsinki, Finland; 1998.
[15] Alava M, Niskanen K. The physics of paper. Rep Prog Phys 2006;69:669–723.
[16] Bronkhorst CA, Bennett KA. Deformation and failure behavior of paper. In: Mark RE, Habeger Jr CC, Borch J, Bruce Lyne M, editors. Handbook of physical testing of paper. Revised and expanded, vol. 1. New York: Marcel Dekker Inc.; 2002. p. 313–427.
[17] Gunderson D, Bendtsen L, Rowlands R. A mechanistic perspective of the biaxial strength of paperboard. J Eng Mater – T ASME 1986;108:135–40.
[18] Rowland R, Gunderson D, Suhling J, Johnson M. Biaxial strength of paperboard predicted by Hill-type theories. J Strain Anal Eng 1985;20(2):121–7.
[19] Suhling J, Rowlands R, Johnson M, Gunderson D. Tensorial strength analysis of paperboard. Exp Mech 1985;25:75–84.
[20] Sunderland P. Measurement and prediction techniques for internal stresses in polymers and composites. PhD thesis. École Polytechnique Fédérale de Lausanne (EPFL), Lausanne, Switzerland; 1997.
[21] Röll K. Analysis of stress and strain distribution in thin films and substrates. J Appl Phys 1976;47:3224–9.
[22] Vacher P, Dumoulin S, Morestin F, Mguil-Touchal S. Bidimensional strain measurement using digital images. Inst Mech Eng Part C ImechE 1999;213:811–7.
[23] Viguié J, Dumont PJJ, Desloges I, Mauret E. Some experimental aspects of the compression behaviour of boxes made up of G-flute corrugated boards. Packag Technol Sci 2010;23:69–89.